INL/JOU-22-67042-Revision-0

Enhanced diffusion bonding of alloy 617 using electric field-assisted sintering

October 2023

Changing the World's Energy Future

Xinchang Zhang, Jorgen Fredrick Rufner, Michael D McMurtrey, Ninad Mohale, Ryann Elizabeth Bass, Tate Patterson, Thomas M. Lillo

Idaho National Laboratory

INL is a U.S. Department of Energy National Laboratory operated by Battelle Energy Alliance, LLC

DISCLAIMER

This information was prepared as an account of work sponsored by an agency of the U.S. Government. Neither the U.S. Government nor any agency thereof, nor any of their employees, makes any warranty, expressed or implied, or assumes any legal liability or responsibility for the accuracy, completeness, or usefulness, of any information, apparatus, product, or process disclosed, or represents that its use would not infringe privately owned rights. References herein to any specific commercial product, process, or service by trade name, trade mark, manufacturer, or otherwise, does not necessarily constitute or imply its endorsement, recommendation, or favoring by the U.S. Government or any agency thereof. The views and opinions of authors expressed herein do not necessarily state or reflect those of the U.S. Government or any agency thereof.

INL/JOU-22-67042-Revision-0

Enhanced diffusion bonding of alloy 617 using electric field-assisted sintering

Xinchang Zhang, Jorgen Fredrick Rufner, Michael D McMurtrey, Ninad Mohale, Ryann Elizabeth Bass, Tate Patterson, Thomas M. Lillo

October 2023

Idaho National Laboratory
Idaho Falls, Idaho 83415

http://www.inl.gov

Prepared for the
U.S. Department of Energy
Under DOE Idaho Operations Office
Contract DE-AC07-05ID14517, DE-AC07-05ID14517

JOURNAL OF MATERIALS RESEARCH AND TECHNOLOGY 2023;26:7033–7051

Available online at www.sciencedirect.com

jmr&t
Journal of Materials Research and Technology

journal homepage: www.elsevier.com/locate/jmrt

Enhanced diffusion bonding of alloy 617 using electric field-assisted sintering

*Xinchang Zhang**, *Michael D. McMurtrey, Ryann E. Bass, Tate Patterson, Ninad Mohale, Thomas M. Lillo, Jorgen F. Rufner*

Idaho National Laboratory, Idaho Falls, ID 83415, United States

ARTICLE INFO

Article history:
Received 18 July 2023
Accepted 9 September 2023
Available online 14 September 2023

Keywords:
Diffusion bonding
Electric-field-assisted sintering
Hot pressing
Alloy 617
Compact heat exchangers

ABSTRACT

The development of compact heat exchangers (CHXs) has gained increasing interest in many industries owing to their high thermal efficiency and reduced size. Diffusion bonding (DB) is an advantageous technique for fabricating CHXs. Alloy 617 is a candidate for manufacturing CHXs for high-temperature advanced nuclear reactors due to its elevated-temperature properties. Previous endeavors in DB of Alloy 617 were conducted by hot pressing (HP), which reported precipitates at the diffusion-bond interface, limited grain boundary (GB) migration, and significantly reduced high-temperature mechanical properties. To overcome these challenges, this study investigated DB of Alloy 617 using electric field-assisted sintering (EFAS). Stacks composed of three sheets were bonded with EFAS using different temperatures, pressures, and hold times. DB using HP as the zero-current analog of EFAS was also performed for comparison. The result shows that Cr- and Mo-rich precipitates were formed at the interface of the hot-pressed samples. The electric current and temperature in EFAS play a significant role in precipitation and GB migration. The electric current coupled with correct temperatures can effectively prevent precipitate formation at the interface and achieve excellent GB migration. Nanoscale Al-rich oxide was formed at the interface of the samples made by both HP and EFAS, but grain boundaries can ignore the nanoscale Al-oxide and migrate across the interface. The temperature, pressure, and hold time also affected diffusion. The temperature is a prerequisite for a successful GB migration, and GB migration can be enhanced by increasing pressure and hold time.

© 2023 The Author(s). Published by Elsevier B.V. This is an open access article under the CC BY-NC-ND license (http://creativecommons.org/licenses/by-nc-nd/4.0/).

1. Introduction

Compact heat exchangers (CHXs) have attracted considerable interest in many industries including nuclear, solar, and fossil fuel because of their uniqueness including reduced size, large heat transfer area-to-volume ratio, and high heat transfer coefficient [1]. The interest in CHXs has advanced the development of many compact-type heat exchangers including plate-fin heat exchanger (PFHE), unit cell heat exchanger (UCHE), and printed circuit heat exchanger (PCHE). Among the available techniques, diffusion bonding (DB) is particularly suitable to manufacture CHXs. DB is a solid-state joining technique in which materials are joined at high temperatures under pressure by atomic diffusion across the mating surfaces [2]. DB is capable of joining similar and

* Corresponding author.
E-mail address: xinchang.zhang@inl.gov (X. Zhang).
https://doi.org/10.1016/j.jmrt.2023.09.080
2238-7854/© 2023 The Author(s). Published by Elsevier B.V. This is an open access article under the CC BY-NC-ND license (http://creativecommons.org/licenses/by-nc-nd/4.0/).

dissimilar metals, such as nickel alloy 800H [3], nickel alloy GH4099 [4], titanium alloy/stainless steel [5], copper alloy/nickel alloy [6], and stainless steel/copper [7]. For fabricating CHXs, many sheets with cooling channels are welded via DB.

Alloy 617 is the leading candidate for fabricating CHXs for high-temperature nuclear applications owing to its good resistance to corrosion, creep, creep-fatigue, and elevated temperature strength [8]. There have been many endeavors in DB of Alloy 617 using hot pressing (HP) [8–18]. Sah et al. [12] studied the microstructure and high-temperature mechanical properties of Alloy 617 hot-pressed at 1150 °C for 2 h under a uniaxial pressure of 14.7 MPa. The results showed limited grain boundary (GB) migration across the interface. This poor GB migration was often reported in DB of Alloy 617 using HP [8,10,13,16,19]. Such unsatisfactory GB migration was often attributed to the extensive Cr-rich carbides and Al-rich oxide along the interface, which inhibited atomic diffusion across the interface [12]. Microstructural discontinuities are detrimental to the mechanical properties. This is evidenced by the noticeable reduction of rupture strength of the diffusion weldment compared to that of the wrought metal [10]. Due to the extensive precipitates and limited GB migration, hot-pressed Alloy 617 was found to have significantly reduced creep performance [10]. Mylavarapu et al. [13] utilized a 2.5 μm thick pure nickel interlayer to bond Alloy 617 plates. Nevertheless, microstructural discontinuities were still seen at the interface with no noticeable GB migration. The nickel interlayer also caused secondary phase particles and pores at the interface, which weakened the bonding strength. Post-bond heat treatment at certain temperatures could achieve some GB migration, but this process has limitations such as inefficiency, geometric distortion, oxidation, and difficulties for large diffusion-bonded stacks [8].

Recently, electric field-assisted sintering (EFAS) has emerged as an efficient approach to consolidating materials. The main characteristic of EFAS is that an electric current flows through the die assembly and the sample (if conductive) [20]. This is significantly different from HP where no current passes through the sample. Because of the current, the die assembly is heated by Joule heating. This unique characteristic of EFAS enables exceptionally rapid heating of the sample and a short processing time. This prevents undesirable grain growth and detrimental phase transformation which were observed in HP due to an extended hold time [20]. As an advanced powder metallurgy technique, EFAS has been widely studied in sintering powdered materials. A few examples include SS316L [21], Inconel 718 [22], Fe-30%Ni alloy [23], and Ti2AlC/TiAl composites [24]. EFAS was also adopted to join metal sheets/rods, such as stainless steel 316 L [25], Ti-45Al-7Nb-0.3W alloy [26], and Titanium/SS304L [27].

EFAS involves a complex multi-physical field including electric, temperature, and pressure fields. The underlying mechanism of their interactions and corresponding effects on the EFAS process is quite complex. The complex fields in EFAS can achieve microstructure and properties quite different from those made by conventional HP. For example, the current can clean surface impurities and oxide layers and thus enhance the bonding strength [28]. Studies also show that not only the temperature but the current can also promote atomic diffusion between the mating materials [29,30]. The high-density current can enhance vacancy defect migration and thus improve the diffusion coefficient [31]. The current was also found to reduce the yield strength of materials and contribute to a rapid consolidation [32]. The combination of current and temperature has large effects on grain growth and solid-state phase transformation [33,34]. However, to date, no consensus has been reached about the heating mechanisms and the effect of electric current in EFAS [20]. Various materials may show different behaviors, and their behaviors are closely related to the EFAS parameters. For example, direct current is favorable for the densification of Ti [35] and WC ceramic [36], but alternating current can avoid macroscopic defects in $BiFeO_3$ [37]. However, the physical interactions of EFAS and optimized parameters for different material systems are unknown and need further exploration.

Due to the unique multi-physical field in EFAS, studies have shown favorable outcomes using EFAS in processing materials. However, to date, DB of Alloy 617 via EFAS has not been reported. As mentioned, Alloy 617 fabricated by HP was found to have extensive precipitates at the interface and limited grain growth across the interface, which largely decreased its mechanical properties. Controlling precipitation at the interface in order to obtain substantial GB migration across the interface in diffusion-bonded Alloy 617 is likely the key to achieving properties equivalent to the base metal. This study hypothesized that the electric current applied during EFAS would minimize precipitate formation and result in improved GB migration. To test this hypothesis, DB of Alloy 617 sheets was carried out using EFAS with different parameters. DB of Alloy 617 using HP was also performed for comparison. The welded samples were characterized in terms of deformation, precipitation, grain growth, and GB migration across the interface. The effects of EFAS parameters especially the electric current on the properties of the diffusion-bonded Alloy 617 were revealed.

2. Materials and experimental method

2.1. *Materials*

Welds were completed using Alloy 617 sheets in the solution-annealed condition with a thickness of 1.6 mm. These Alloy 617 sheets were procured from High Temp Metals, Inc. (USA). Table 1 lists the chemical composition of Alloy 617, which satisfies the American Society for Testing and Materials (ASTM) B168-11 specifications. The sheets were sectioned to 14.14 mm × 14.14 mm coupons for DB.

Before DB, both surfaces of the square coupons were mechanically ground using SiC abrasive papers up to 800 grit to achieve flat and parallel surfaces as well as to remove surface oxides, defects, and contaminations. The prepared sheets were cleaned with acetone in an ultrasonic bath for 10 min, cleaned with ethanol, and finally air-dried. The surface roughness of three random sheets was measured using a Veeco profilometer. Measurements show a peak *Ra* of 0.029 μm and *Rz* of 0.97 μm. Three coupons were stacked together and loaded into a 20-mm inner diameter graphite die for DB. The square sample was smaller than the die cavity, which allowed unconstrained compression during DB

Table 1 – Chemical composition of the Alloy 617 sheets and chemistry requirement specified in ASTM B168-11 (wt.%).

Element		Ni	Cr	Co	Mo	Al	C	Fe	Mn	Si	S	Ti	Cu	B	P
Alloy 617		52.5	21.8	12.9	9.6	1.13	0.09	1.17	0.08	0.07	0.001	0.38	0.04	0.004	0.006
ASTM B168-11	Min	44.5	20.0	10.0	8.0	0.8	0.05	–	–	–	–	–	–	–	N/A
	Max	–	24.0	15.0	10.0	1.5	0.15	3.0	1.0	1.0	0.015	0.6	0.5	0.006	

(material flow in the direction perpendicular to the applied force due to creep and/or yielding at the bonding temperature). Graphite foils with a thickness of 0.127 mm were placed in the contacting surfaces of the die assembly for easy removal of the sample after the experiment.

2.2. *EFAS experimental procedure*

DB of Alloy 617 via EFAS was achieved using a Direct Current Sintering Furnace DCS-5 from Thermal Technology, LLC. (USA). The DCS-5 is capable of operating at a peak temperature of 2500 °C, a maximum applied force of 50 kN, and a peak electric current of 2000A. Fig. 1a illustrates the schematic of the EFAS process. During EFAS, the electric current initiated from the positive electrode can pass through the die-punch as well as the sample due to the good electrical conductivity of Alloy 617. The heating mechanism is Joule heating. Fig. 1c shows an example of the evolution of critical parameters including temperature, applied pressure, current intensity, and hydraulic ram position during EFAS. In the beginning, the DCS-5 chamber was evacuated to 2×10^{-2} torr and backfilled with argon gas. Subsequently, uniaxial pressure was applied and gradually increased to the target pressure. Next, an electric current was applied to heat the die assembly to 300 °C and held for 1 min so that the pyrometer can capture the temperature. After the hold, the electric current was increased and the die assembly was heated to the target temperature at a rate of 100 °C/min. Pressure and temperature were kept constant during the dwelling stage. After dwell, the current and pressure were released. Consequently, the sample cooled down to room temperature in the chamber at ~200 °C/min. DB via EFAS was performed at temperatures of 1050 °C, 1100 °C

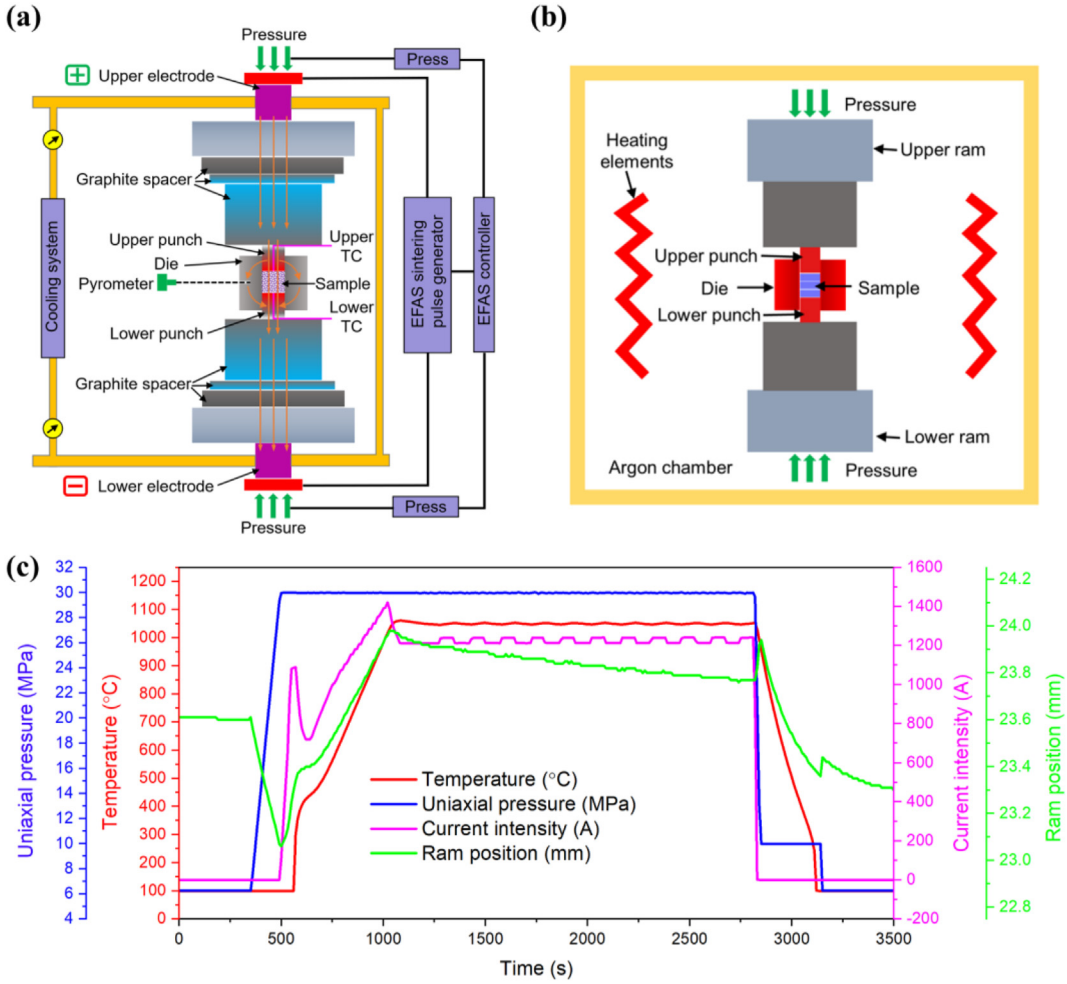

Fig. 1 – Schematics of (a) EFAS and (b) HP. (c) Evolution of temperature, uniaxial pressure, current intensity, and ram position during DB using EFAS.

and 1150 °C; pressure of 10 MPa, 20 MPa and 30 MPa; and hold time of 10 min, 30 min and 90 min, as tabulated in Table 2. The total electric current flowing through the die assembly was 1240A, 1322A, and 1377A for the temperature of 1050 °C, 1100 °C, and 1150 °C, respectively. The current passing through the sample, however, depends on several factors including the material properties, punch and die geometries, and sample size, and therefore, cannot be quantified experimentally.

During EFAS, the temperature was monitored using a pyrometer aimed at a hole in the graphite die. Sample temperature was measured by two type C thermocouples running through the upper and lower punches (Fig. 2a). Due to the Joule heating mechanism, a temperature gradient can exist in the die assembly. As a result, the sample temperature could be different from the temperature measured by the pyrometer. Temperature is a critical factor in DB and the sample temperature and pyrometer reading during EFAS at 1150 °C are plotted in Fig. 2a. This plot shows the temperature gradient within the die assembly. The temperature on the sample surface was close to 1200 °C, which is about 50 °C higher than the pyrometer reading (1150 °C).

2.3. *HP experimental procedure*

DB using HP was carried out as a zero-current analog of EFAS for comparison. HP experiments were conducted using an Oxy-Gon hot press furnace in an argon environment. Fig. 1b shows the schematic of the HP process. During HP, the sample in the graphite die was subjected to uniaxial pressure and elevated temperature at the same time. The sample was heated by traditional resistive heating in the HP furnace while compressed by upper and lower hydraulic rams. No electric current passed through the sample during HP. DB using HP was performed under pressures of 20 MPa and 30 MPa; hold time of 30 min and 90 min; and temperatures of 1150 °C and 1200 °C, as listed in Table 2. Due to the elevated temperature at sample surface (1200 °C) during EFAS at pyrometer set point of 1150 °C, DB at 1200 °C using HP functioned better comparison to the samples fabricated at 1150 °C by EFAS. The heating rate during HP was set at 20 °C/min. Subsequent cooling of the samples was conducted in the hot press chamber with an uncontrolled cooling rate of ~50 °C/min.

Table 2 – Design matrix for DB of Alloy 617 via EFAS and HP.

Process	Temperature (°C)	Pressure (MPa)	Hold time (min)	Sample ID
HP	1150	20	90	HP-#1
	1200	20	90	HP-#2
	1150	30	30	HP-#3
	1200	30	30	HP-#4
EFAS	1050	30	30	EFAS-#1
	1100	30	10	EFAS-#2
	1100	30	30	EFAS-#3
	1150	10	30	EFAS-#4
	1150	20	10	EFAS-#5
	1150	20	30	EFAS-#6
	1150	20	90	EFAS-#7
	1150	30	30	EFAS-#8

2.4. *Material characterization*

The samples were sectioned to reveal the DB interfaces. The sectioned samples were mounted in Bakelite and mechanically ground and polished following standard metallography procedures. Vibratory polishing was carried out in 0.02 μm colloidal silica suspension for ~4 h. The bonded interfaces were inspected using a light optical microscope (Keyence VHX6000) and a scanning electron microscope (SEM) (FEI Quanta FEG 650) equipped with energy-dispersive X-ray spectroscopy (EDS) and electron-backscattered diffraction (EBSD). EBSD maps were captured with a step size of 2 μm. The EBSD data was post-processed in OIM Analysis software. Data with less than a 0.1 confidence index was removed from the data set. The grain size of the samples was measured. Grains were defined as a minimum of 5 pixels. A grain boundary was defined as a misorientation angle of 5° between neighboring pixels. GB migration across the interface was quantified as the percentage of the lengths of interface with GB migration compared to the total length of the interface, as illustrated in Fig. 2b. Optical micrographs were taken over the entire length of both interfaces and the summation of both interfaces was used to quantify the GB migration. Grain boundaries were revealed with a 10% oxalic electrochemical etch at 2.2 V for 30 s. To characterize the fine precipitates of the diffusion-bonded Alloy 617, characterization using transmission electron microscopy (TEM) was performed. Lift-out samples for TEM analysis were prepared using the FEI Contra 3D FEG dual-beam focused ion beam (FIB) microscope. TEM imaging and EDS analysis were performed using FEI Tecnai TF30-FEG STwin TEM.

3. Results

3.1. *Microstructure of the as-received alloy 617*

Fig. 3a and b shows back-scattered-electron (BSE) images of the as-received Alloy 617 taken at 500 × and 2000 × , respectively. The solution-annealed Alloy 617 shows an equiaxed structure with annealing twins (Fig. 3a). A small number of primary precipitates can be observed in the as-received state (Fig. 3b). These precipitates were identified as mostly Cr- and Mo-rich carbides and a small quantity of titanium-rich carbonitride Ti(C,N). This agrees with the findings reported earlier [38,39]. No substantial quantity of precipitates was seen within the grains and along grain boundaries in the as-received material. Fig. 3c and d shows the EBSD inverse pole figure (IPF) and grain size statistics of the as-received Alloy 617. Equiaxed grains with a grain size of 48 ± 18 μm were identified.

3.2. *Microstructure of alloy 617 fabricated via HP*

Fig. 4 shows light optical microscopy (LOM) images taken at the center of the samples fabricated by HP. The brackets in these images indicate the location of the interface.

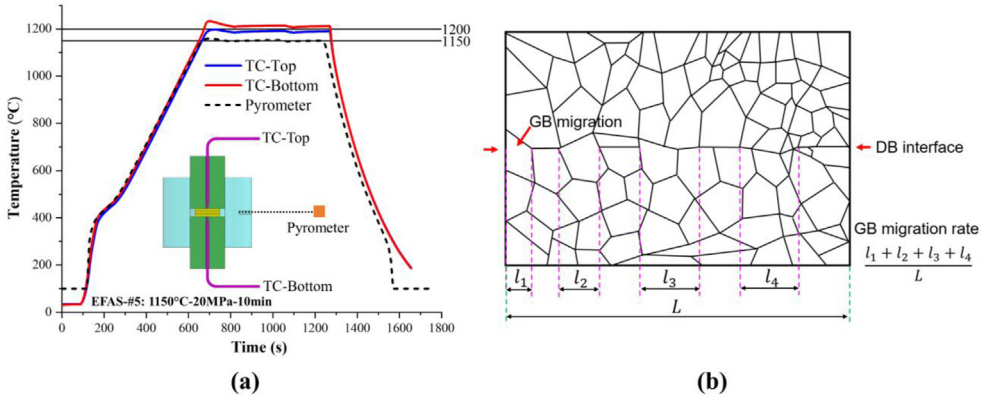

Fig. 2 – (a) Temperature recorded by TC and pyrometer during EFAS at 1150°C-20MPa-10min. (b) Schematic diagram illustrating the statistical method of GB migration rate.

Examination shows the Alloy 617 sheets had been bonded successfully, except HP-#3 where pores were observed at the interface (Fig. 4c). HP-#1, #2, and #4 are free of defects at the interface. Uniaxial deformation of the samples is 19.4%, 22.1%, 19.1%, and 34.4% for the HP-#1, #2, #3, and #4, respectively. The yield strength of Alloy 617 at temperatures above 1100 °C is below 10 MPa [40]. Therefore, the applied load during HP exceeded the yield strength of Alloy 617 at the bonding temperature and thus, was responsible for the plastic deformation of the samples. It is worth mentioning that HP-#4 deformed significantly and was extruded to the die walls creating a coin-like shape. This level of plastic deformation should be prevented as it damages the geometries of the micro-channels for heat exchanger applications. Due to the large plastic deformation and loss of geometry in HP-#4, the corresponding parameters are not appropriate for DB of CHXs.

Fig. 5 shows BSE micrographs over the interface of the hot-pressed Alloy 617. In the as-bonded condition, the microstructure of the Alloy 617 hot-pressed at 1150 °C (Fig. 5a and c) has been altered compared with the as-received material (Fig. 3a). The presence of a considerable amount of intergranular and intragranular precipitates was the most significant change after HP at 1150 °C. EDS analysis confirms these precipitates were mostly Cr- and Mo-rich carbides and oxides

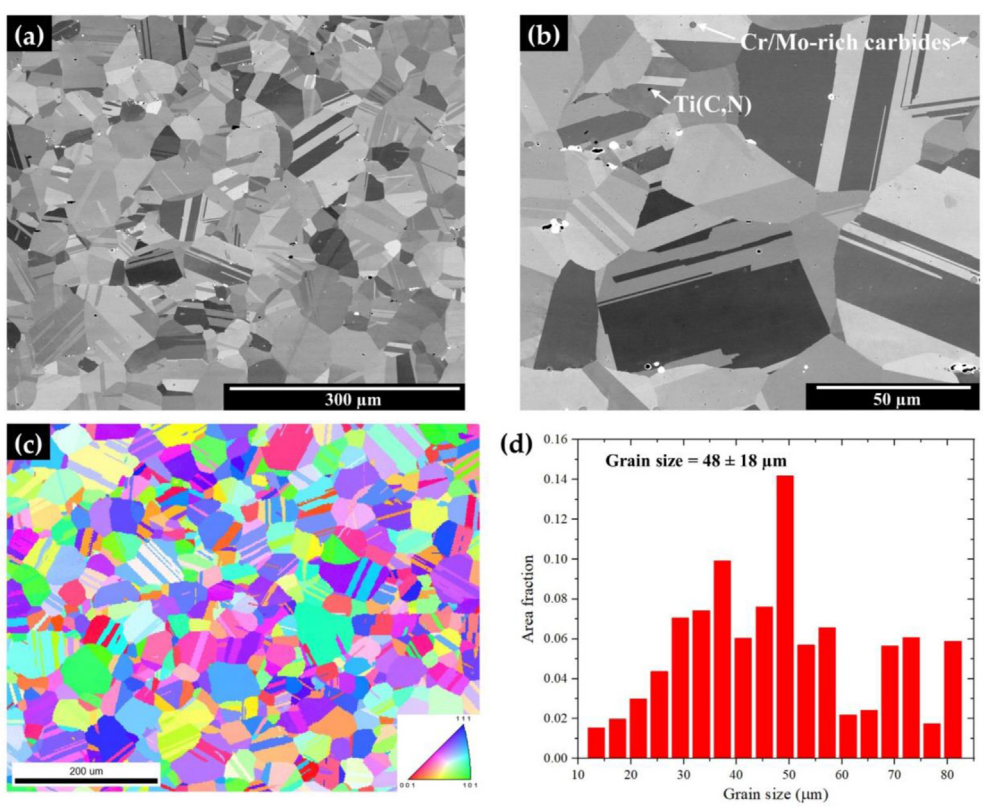

Fig. 3 – BSE micrographs of the as-received Alloy 617 taken at (a) 500 × and (b) 2000 × . (c) IPF and (d) grain size statistics of the as-received Alloy 617.

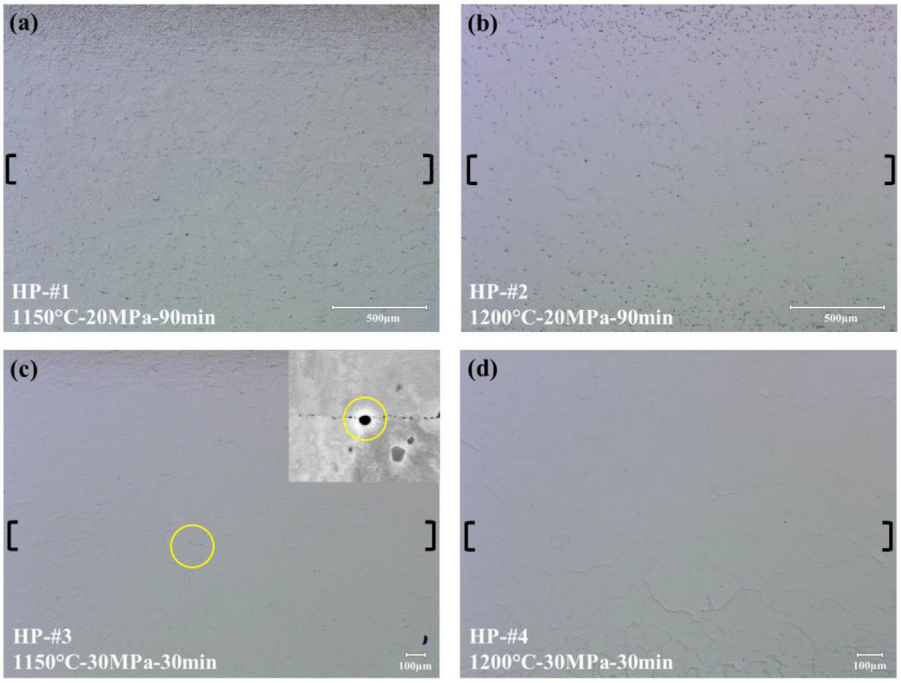

Fig. 4 – LOM images of (a) HP-#1, (b) HP-#2, (c) HP-#3, and (d) HP-#4. Brackets indicate the location of the DB interface.

with some scattered Ti(C,N), as evidenced in Fig. 6. It is worth noticing that the as-bonded Alloy 617 also shows fine precipitates at the DB interface as depicted in Figs. 5a and 6. The morphology and distribution of precipitates are in good agreement with Alloy 617 fabricated by HP at 1150 °C reported earlier [8,12]. Fig. 7 shows IPF maps and grain size statistics of the samples fabricated by HP. HP-#1 and HP-#3 have a grain size of 140 ± 79 μm and 101 ± 57 μm, respectively. Compared with the as-received material, grain growth occurred after HP at 1150 °C. However, the substantial grain growth did not result in satisfactory GB migration across the interface. A planar bond line is visible as indicated by the arrows in Fig. 5a, c, 7a and 7e. Very limited GB migration, 3.1% and 3.6%, was achieved in HP-#1 and HP-#3, respectively. This agrees with previous studies that limited GB migration across the interface was obtained in hot-pressed Alloy 617 [8,10,13,16,19].

Alloy 617 fabricated at 1200 °C (Fig. 5b and d) shows different microstructure compared with those fabricated at 1150 °C. First, the number of precipitates was significantly reduced in HP-#2 and HP-#4 compared with HP-#1 and #3. Most of the precipitates were dissolved into the matrix. Some precipitates were randomly distributed within the grains and along the grain boundaries. It should be noted that precipitates rich in Cr and Mo remained at the interface (Fig. 8). Second, IPF maps (Fig. 7c and g) reveal the grain size of the samples hot-pressed at 1200 °C is about twice those fabricated at 1150 °C. Third, improved GB migration across the interface was seen in the samples fabricated at 1200 °C. Approximately 24.2% and 53.2% of grains have migrated across the interface in HP-#2 and HP-#4, respectively. However, it needs to be mentioned that 53.2% of GB migration in HP-#4 was obtained at the sacrifice of 34.4% overall plastic deformation and loss of geometry.

3.3. *Microstructure of alloy 617 fabricated via EFAS*

Fig. 9 shows representative LOM images of the as-fabricated Alloy 617 via EFAS (interfaces are indicated by brackets). Unlike hot-pressed samples where pores were observed at the interface of HP-#3, the EFAS samples showed discontinuity-free interfaces at all the fabrication conditions. Under LOM, the interfaces are nearly indistinguishable. With respect to deformation, an overall deformation of 2.8%, 4.8%, 7.1%, 3.1%, 12.8%, 18.1%, 23.2% and 23.1% was measured for EFAS-#1 to #8, respectively. Fig. 10 shows BSE micrographs of the Alloy 617 fabricated by EFAS. Depending on the parameters, different microstructures were formed. EFAS-#1 (Fig. 10a) fabricated at 1050 °C shows a considerable number of precipitates. Similar to HP-#1 and HP-#3 (Fig. 5a and c), these precipitates were mostly Cr- and Mo-rich carbides and oxides, and a few scattered Ti(C,N). These precipitates were also observed along the interface of EFAS-#1. In terms of GB migration, EFAS-#1 shows a distinct planar interface, indicating no GB migration. This unsuccessful GB migration is also confirmed by the IPF map (Fig. 11a). EFAS-#1 did not experience grain growth (Fig. 11b), showing a similar grain size (45 ± 19 μm) as the as-received material (48 ± 19 μm). At the EFAS temperature of 1100 °C (Fig. 10b and c), precipitates remained. Similar to EFAS-#1, precipitates were found in the grains, along the grain boundaries, and at the interface. However, different from EFAS-#1, a few grains started to migrate across the interface in EFAS-#2 and EFAS-#3 (Figs. 10c and 11e). The migration of grain boundaries is more obvious in EFAS-#3 which was fabricated with a longer dwell. Although grains started to migrate at 1100 °C, GB migration is very limited. There is also no grain growth in EFAS-#2 (40 ± 16 μm) and EFAS-#3 (43 ± 19 μm) compared with the as-received material.

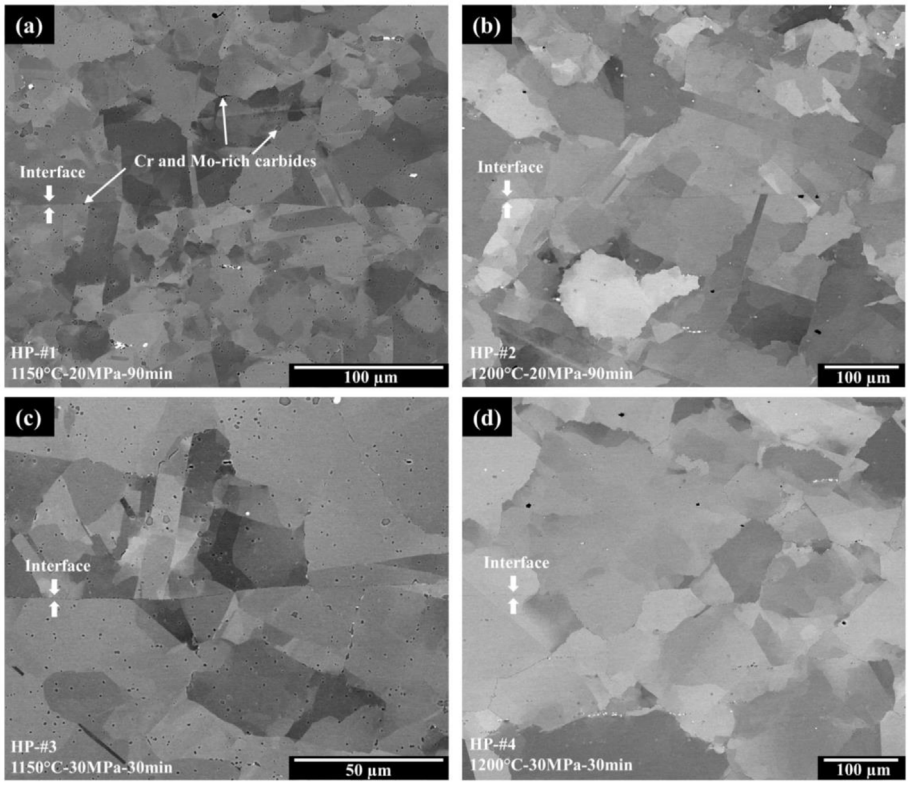

Fig. 5 – BSE micrographs of (a) HP-#1 (1150 °C), (b) HP-#2 (1200 °C), (c) HP-#3 (1150 °C), and (d) HP-#4 (1200 °C). Arrows indicate the location of the DB interfaces.

The samples fabricated at 1150 °C via EFAS (Fig. 10d-h) show a different microstructure compared with those fabricated at 1050 °C and 1100 °C. First, the number of precipitates was significantly reduced at 1150 °C. Only a few precipitates were observed within the grains (Fig. 10d-h), while the grain boundaries and the interfaces were mostly free of precipitates. Second, significant GB migration across the interface was achieved in the EFAS samples fabricated at 1150 °C. BSE micrographs show good migration of grain boundaries across the interface, making the interface barely distinguishable. IPF maps (Figs. 11g and 12a, c, e, g) also support this finding, where a homogeneous equiaxed

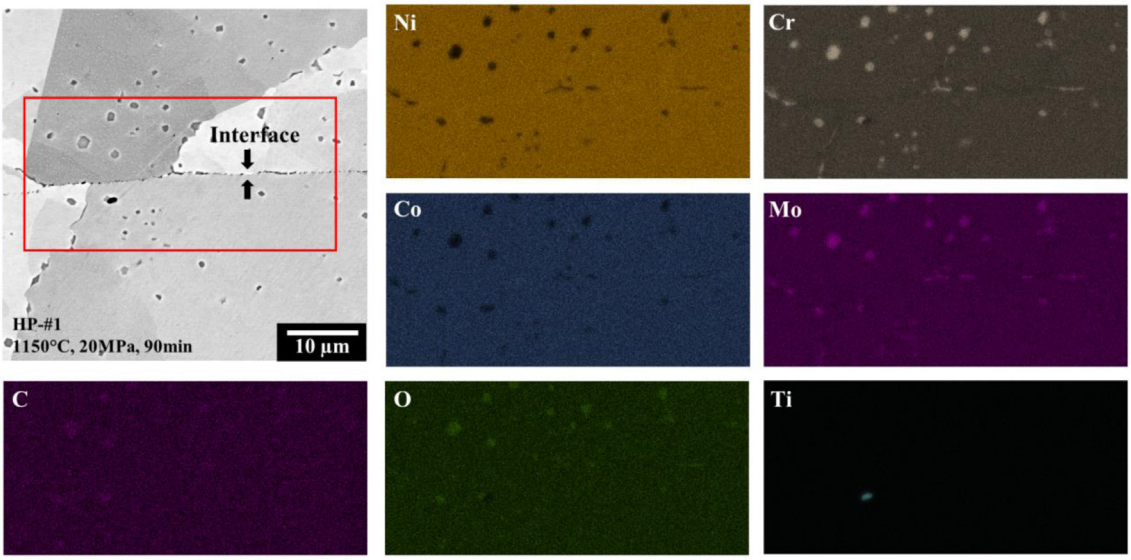

Fig. 6 – EDS maps showing Cr- and Mo-rich carbides and oxides in the grains, along the grain boundaries and at the interface of HP-#1.

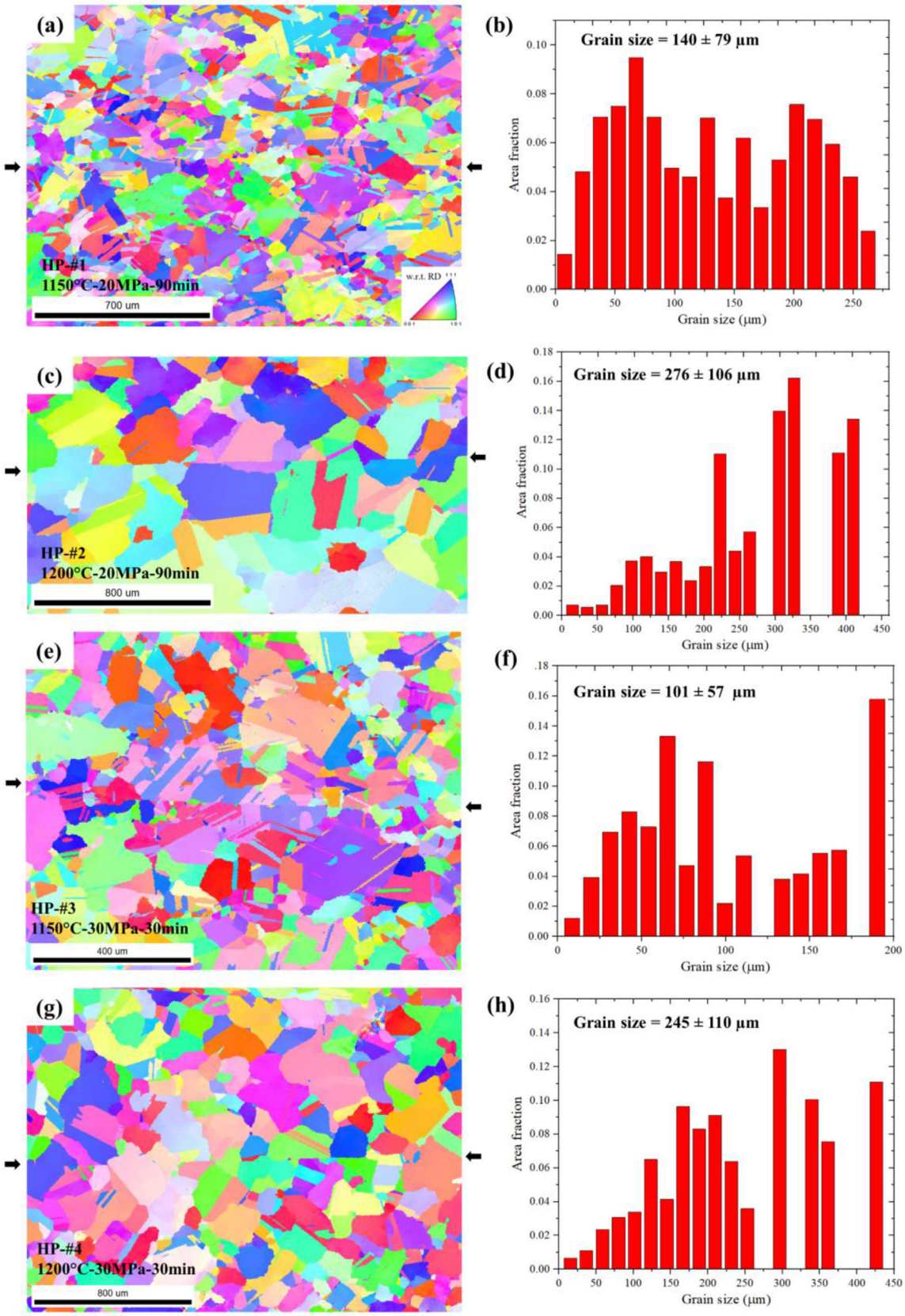

Fig. 7 – EBSD IPF maps (a, c, e, g) and grain size statistics (b, d, f, h) of HP-#1 (a, b), HP-#2 (c, d), HP-#3 (e, f) and HP-#4 (g, h). Arrows indicate the DB interface.

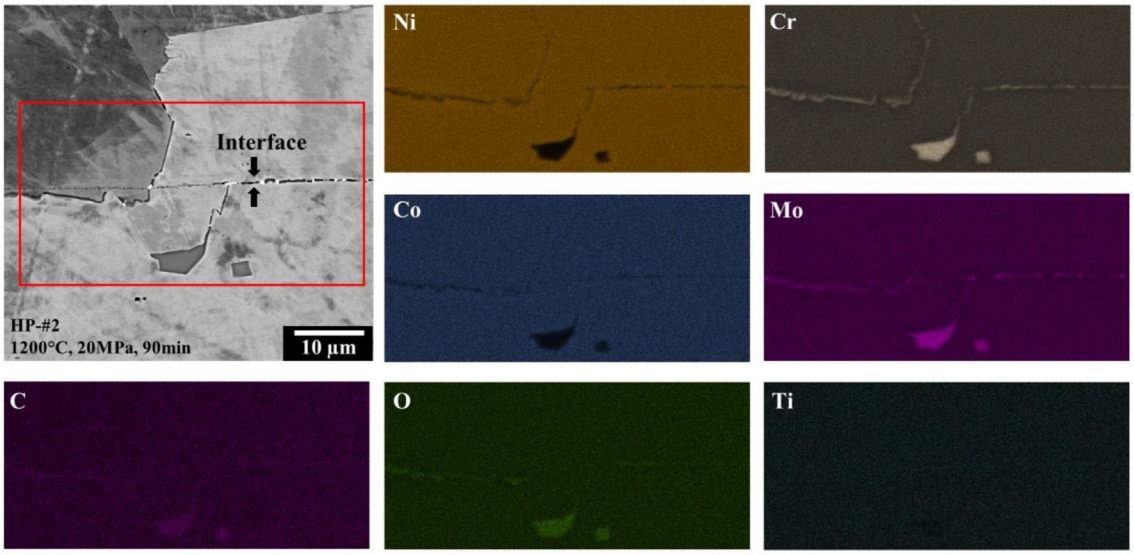

Fig. 8 – EDS maps showing Cr- and Mo-rich carbides and oxides at the interface of the HP-#2.

microstructure was achieved across the interface. Measurements showed 52.7%, 69.7%, 72.6%, 90.1%, and 88.5% of grains successfully migrated over the interface in EFAS-#4, #5, #6, #7, and #8, respectively. Regarding grain growth, the EFAS samples fabricated at 1150 °C experienced remarkable grain growth. Except for the EFAS-#5 which was made at a shorter dwell (10 min) and has a 169 ± 69 μm grain size, other samples have an average grain size ranging from 236 μm to 284 μm, which is about 5 × to 6 × of the grain size of the as-received material.

Fig. 13a shows a high-magnification BSE image at the interface of EFAS-#8. Fine discontinuous features resembling black dots were observed at the interface. They ranged from a few nm to 0.5 μm in size. To identify these fine features, TEM analysis was performed. As shown in Fig. 13b, a lamella across the DB interface was extracted using the FIB technique for TEM characterization. Fig. 13c displays a cross-section of the sample. A TEM micrograph is shown in Fig. 13d. EDS point analysis was conducted on four dots as indicated in Fig. 13d. The strong peaks of Al and O confirm these fine dots are Al-

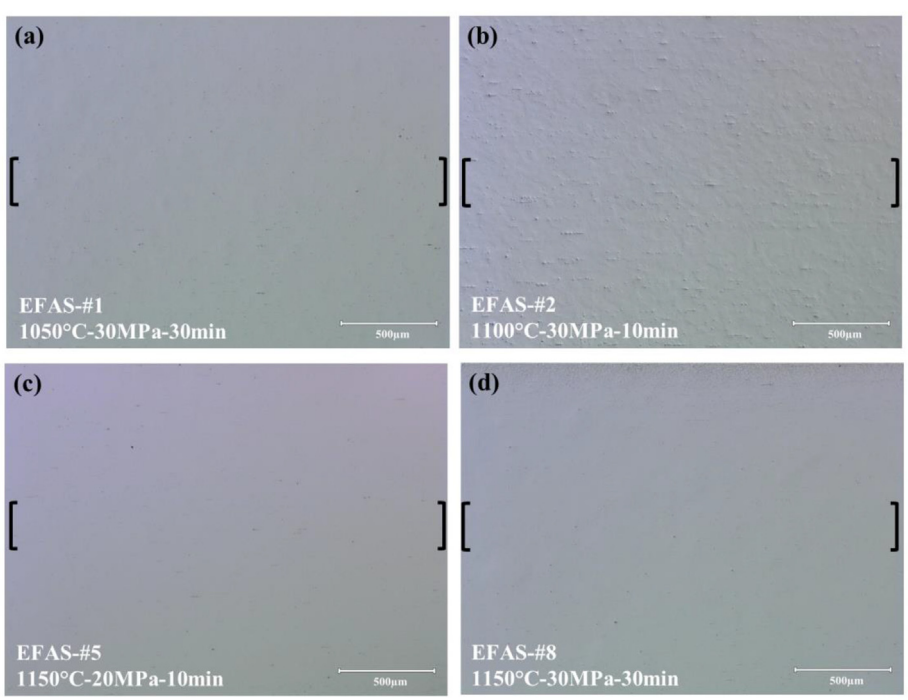

Fig. 9 – Representative LOM images of (a) EFAS-#1, (b) EFAS-#2, (c) EFAS-#5, and (d) EFAS-#8. Brackets indicate the location of the DB interface.

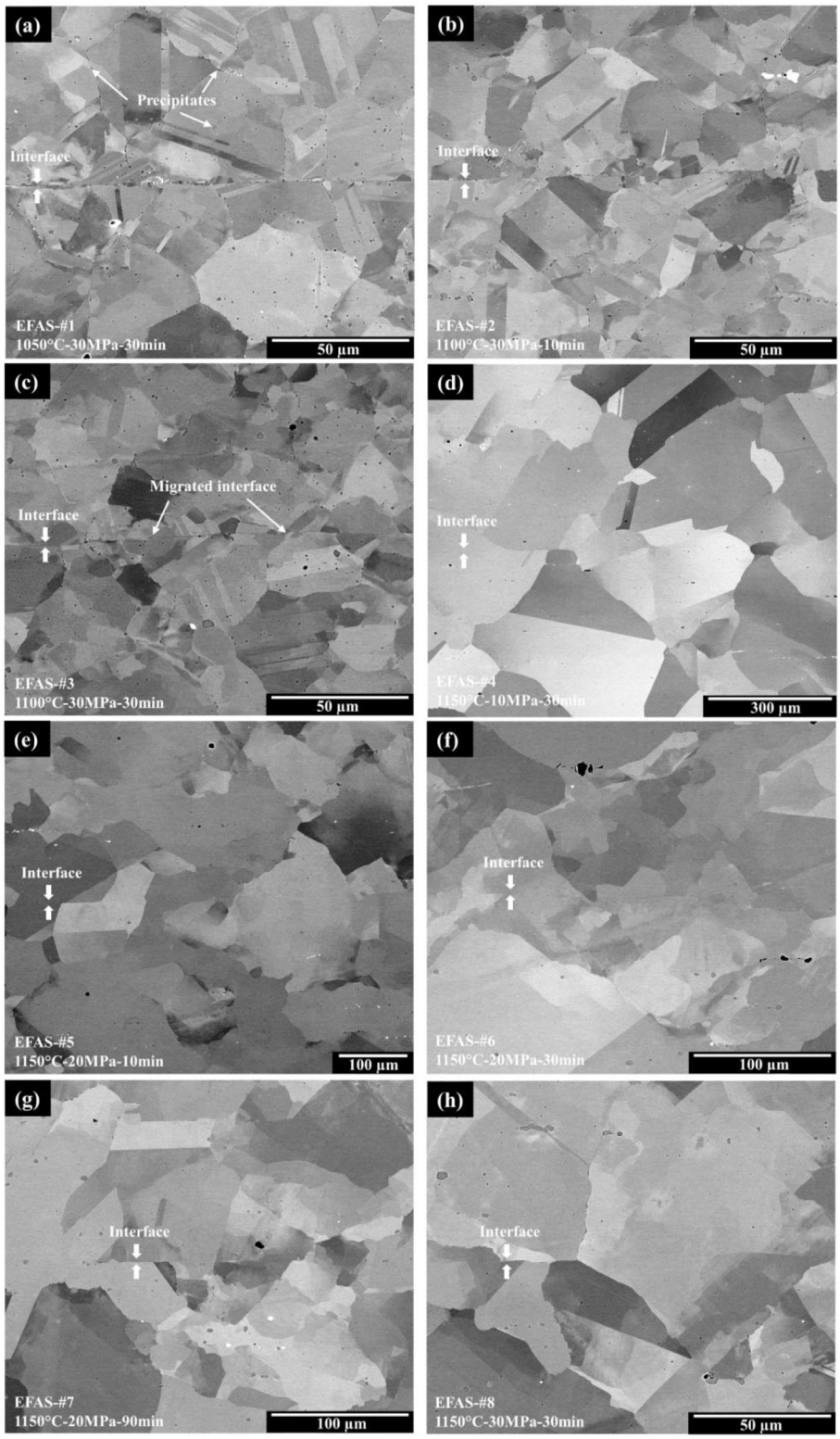

Fig. 10 – BSE micrographs of (a) EFAS-#1, (b) EFAS-#2, (c) EFAS-#3, (d) EFAS-#4, (e) EFAS-#5, (f) EFAS-#6, (g) EFAS-#7, and (h) EFAS-#8. Arrows indicate the DB interface.

rich oxide. EDS mapping was also performed across a random dot as shown in Fig. 13e, which supports the same finding. This finding is in good agreement with the results reported by Sah et al. [12]. Nanoscale Al-rich oxides along the interface were observed in all the EFAS and HP samples, regardless of the electric current and other parameters. It is also worth noticing that the nanoscale Al-rich oxides did not appear to pin the grain boundaries. Instead, they remained at the

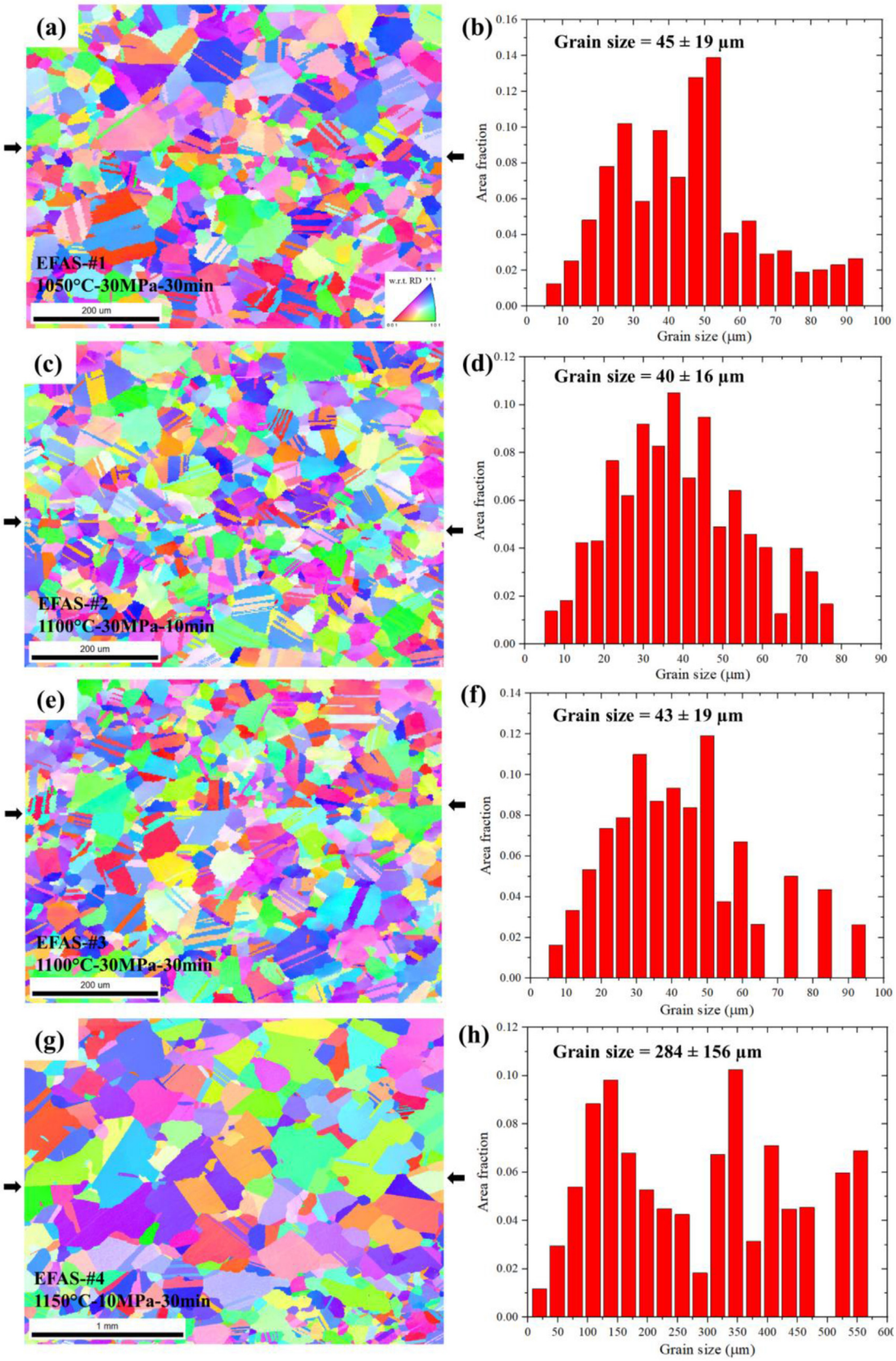

Fig. 11 – EBSD IPF maps (a, c, e, g) and grain size statistics (b, d, f, h) of EFAS-#1 (a, b), EFAS-#2 (c, d), EFAS-#3 (e, f) and EFAS-#4 (g, h). Arrows indicate the DB interface.

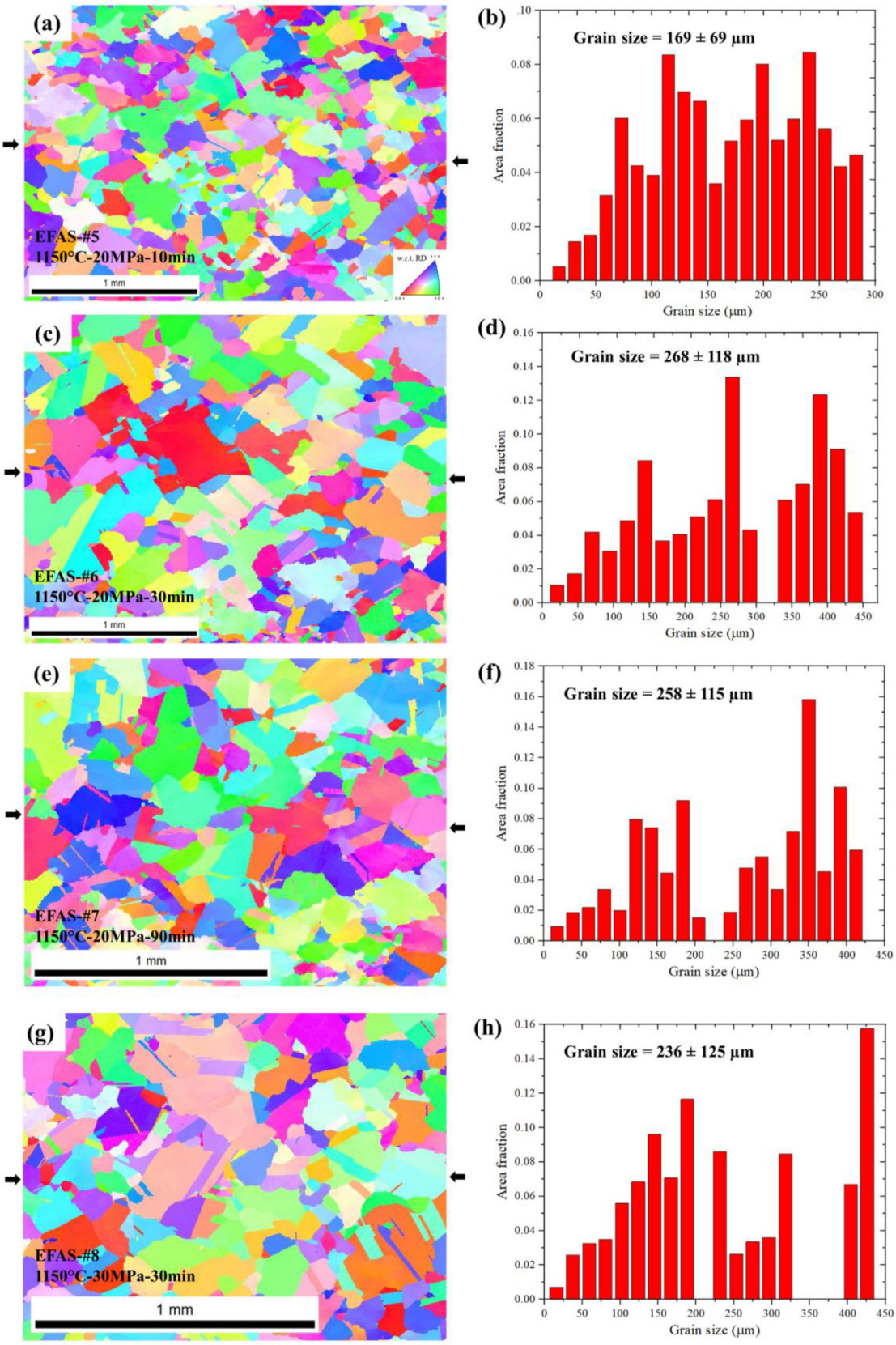

Fig. 12 – EBSD IPF maps (a, c, e, g) and grain size statistics (b, d, f, h) of EFAS-#5 (a, b), EFAS-#6 (c, d), EFAS-#7 (e, f) and EFAS-#8 (g, h). Arrows indicate the DB interface.

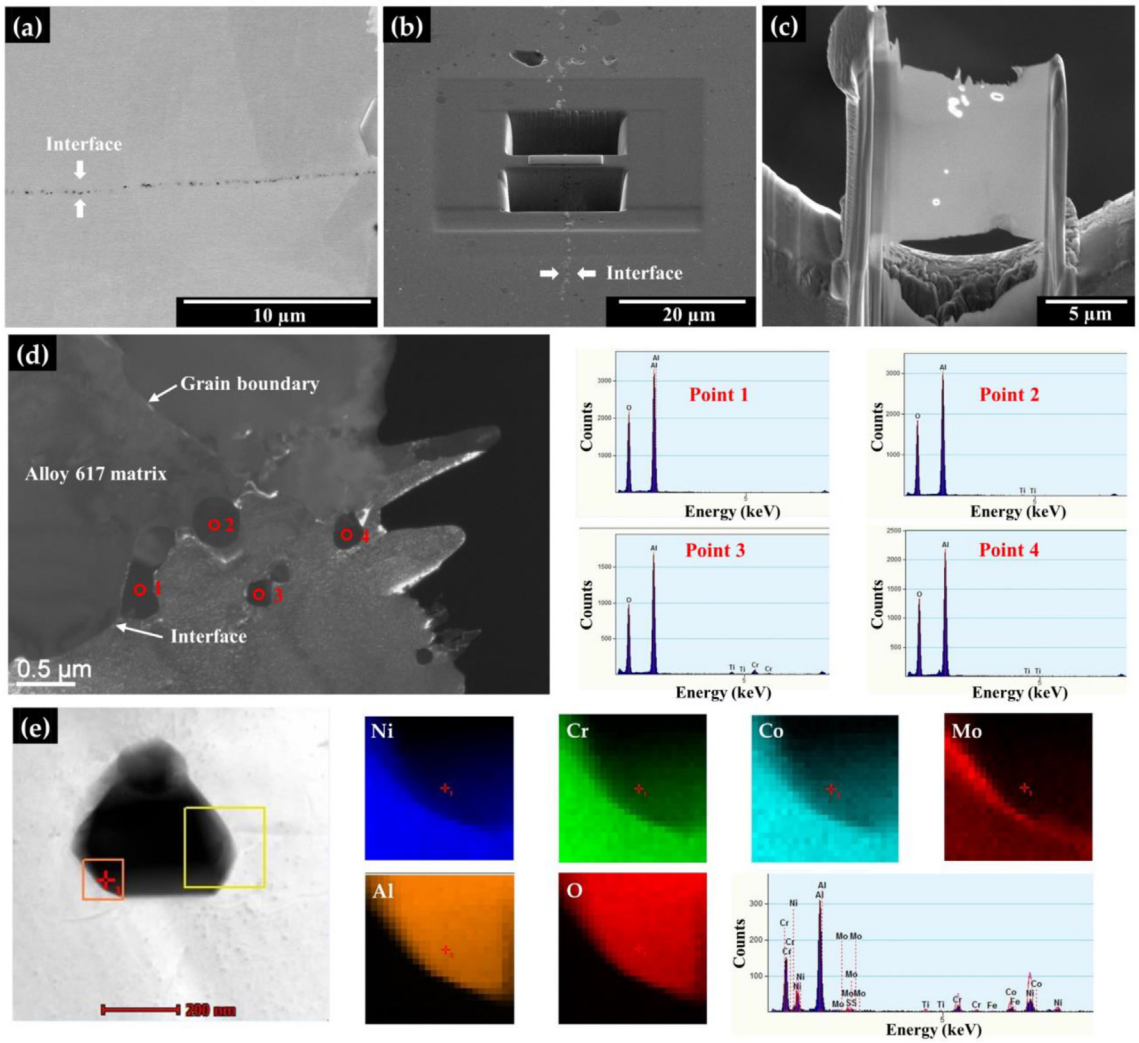

Fig. 13 – (a) High-magnification BSE micrograph at the interface of EFAS-#8. (b) FIB milling location. (c) Prepared sample for TEM analysis. (d) EDS point analysis and (e) mapping results confirming Al-rich oxide.

original interface and ended up within the grain interiors (Fig. 13a).

4. Discussion

4.1. *Inhibition of GB migration in hot-pressed alloy 617*

Table 3 summarizes the diffusion-bonded Alloy 617 fabricated by HP and EFAS. It can be seen that GB migration is not significant in the HP samples. Nickel alloys such as Alloy 617 containing Cr, Mo, and Al are known to form a surface passivation layer. This thin passivation layer mainly consists of oxides of these elements. Although these oxides protect Alloy 617 from oxidation and corrosion, these stable oxides largely restrict elemental diffusion across the interface during DB. Sah et al. [12] reported that hot-pressed Alloy 617 shows an extensive amount of Cr-rich carbides and Al-rich oxides at the interfaces, which were believed to inhibit elemental diffusion across the interface and result in microstructural discontinuities. The precipitates at the interface were also reported to negatively impact the elevated-temperature mechanical properties of diffusion-bonded Alloy 617 [8,10,12]. This study partially agreed with the literature. As shown in Fig. 8, Cr- and Mo-rich precipitates were found along the interface of the hot-pressed samples. Because of these precipitates, limited GB migration was achieved by HP. However, in contrast to the literature, the contribution of nanoscale Al-rich oxide at the interface to restrict GB migration may not be as significant as previously reported. This is due to grain boundaries having sufficient energy to overcome the pining effects of the fine Al-oxide and migrating across the interface, thus, leaving Al-oxide within the grain interiors (Fig. 5b). Grain boundary pining is controlled by particle size and number fraction, and the density and size of the Al-rich nano-particles were not sufficient to pin the grain boundaries. In contrast, the larger Cr- and Mo-rich precipitates are more dominant pining particles.

Diffusion can be divided into three stages: (a) surface diffusion, (2) grain boundary diffusion, and (3) lattice diffusion (or volume diffusion). The energy needed to initiate surface diffusion, grain boundary diffusion, and lattice diffusion is Q_S,

Table 3 – Summary of diffusion-bonded Alloy 617 fabricated by HP and EFAS.

Process	Sample ID	Deformation	Porosity at interface	Cr and Mo Precipitates at interface	GB migration across interface	Grain size (μm)
HP	HP-#1	19.4%	No	Yes	3.1%	140 ± 79
	HP-#2	22.1%	No	Yes	24.2%	276 ± 106
	HP-#3	19.1%	Yes	Yes	3.6%	101 ± 57
	HP-#4	34.4%	No	Yes	53.2%	245 ± 110
EFAS	EFAS-#1	2.8%	No	Yes	No	45 ± 19
	EFAS-#2	4.8%	No	Yes	Insignificant	40 ± 16
	EFAS-#3	7.1%	No	Yes	Insignificant	43 ± 19
	EFAS-#4	3.1%	No	No	52.7%	284 ± 156
	EFAS-#5	12.8%	No	No	69.7%	169 ± 69
	EFAS-#6	18.1%	No	No	72.6%	268 ± 118
	EFAS-#7	23.2%	No	No	90.1%	258 ± 115
	EFAS-#8	23.1%	No	No	88.5%	236 ± 125

Q_{GB}, and Q_L, respectively, and $Q_S < Q_{GB} < Q_L$. DB using HP can be explained by the schematics in Fig. 14. Prior to HP, a few asperities on two mating sheets were in contact (Fig. 14a). Gaps formed at the faying surface due to surface imperfection. A thin passivation layer consisting of oxides exists in Alloy 617. In the second stage (Fig. 14b), the sample was heated up to an elevated temperature and thus plastic deformation occurred under the applied uniaxial pressure. The deformation induced interfacial boundary formation and eliminated most pores at the interface. However, a few pores are still entrapped at the interface. In the next stage (Fig. 14c), the remaining pores are eliminated by surface and grain boundary diffusion. However, lattice diffusion was not the dominant diffusion mechanism at this stage since it requires higher energy. HP-#1 is at this stage. At the final stage, lattice diffusion became significant relative to surface and grain boundary diffusion, causing grain boundaries to migrate over the interface. The samples hot-pressed at 1200 °C (HP-#2 and #4) are at this stage. However, the Cr- and Mo-rich precipitates at the interface largely restricted GB migration, although the nanoscale Al-rich precipitates did not impede the movement of grain boundaries. Controlling precipitates on the faying surfaces of Alloy 617 before or during DB is important to yield better GB migration. This was confirmed with a pre-oxidation of Alloy 617 sheets at 930 °C for 200 h in ambient air [9]. An ~20 μm layer was removed from the surface and a Cr-, Al- and Ti-depleted zone was obtained [9]. DB using HP was performed on those sheets and untreated sheets. Compared to untreated material, precipitates at the interface were largely removed in the treated sheets and GB migration was improved [9].

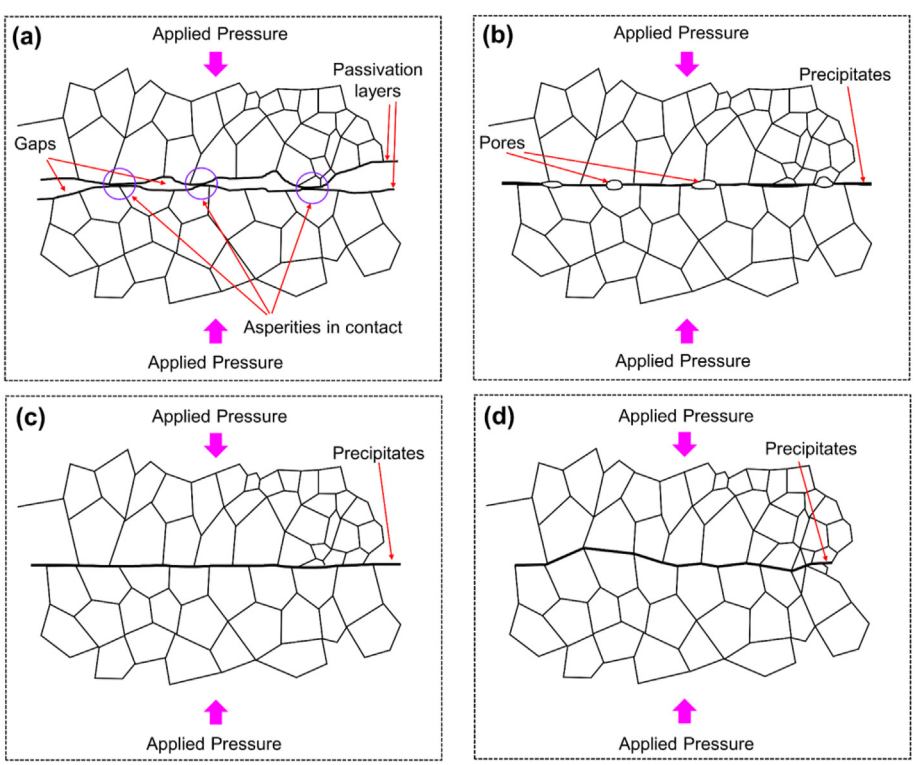

Fig. 14 – Schematic of DB using HP in the stage of (a) initial asperity contact, (b) boundary formation, (c) pore elimination, and (d) lattice diffusion and GB migration.

4.2. *Importance of applied electric current in DB of alloy 617*

A difference in microstructure was observed in the EFAS and HP samples made at equivalent conditions. First, in contrast to HP samples where precipitates remained at the interface (Fig. 8), precipitates were not observed at the interface of the EFAS samples fabricated at 1150 °C. Second, enhanced GB migration in the EFAS samples was seen compared with HP. Considering both the EFAS and HP experiments were conducted under equivalent conditions, the difference in GB migration between the EFAS and HP samples is believed to be a consequence of the applied electric current.

The contribution of electric current to GB migration is suspected to be due to (1) impediment of precipitation at the interface, (2) improved atomic diffusion by enhancing vacancy defect migration, and (3) dielectric breakdown of surface oxides. As discussed earlier, a significant difference between HP and EFAS samples is the absence of precipitation at the interface of the EFAS samples made at 1150 °C. Electric current was reported to have large effects on precipitation. The influence of an electric current on precipitation depends on many factors including material composition, material properties, solutionizing temperature, current density, current frequency, processing time, and temperature [20]. Depending on these factors, electric current was reported to either accelerate or retard precipitation during EFAS. For instance, Kapoor et al. [33] studied maraging steel (Fe-18Ni-11.6Co-3.6Mo-1.2Ti-0.13Al in wt.%) under a pulsed electric current at current densities ranging from 4 to 10 kA/mm^2. The authors revealed that Ni_3(Ti, Mo) precipitation occurred under certain conditions. It was believed that the electric current flowing through the material reduced the activation energy of precipitation and thus accelerated precipitation. In contrast, Onodera and Hirano [41] reported retarding effect of direct electric current on precipitation in bulk Al-4 wt.% Cu alloy. This retarding effect was also observed by Shine and Herd for the same alloy system [42]. At this time, understanding the complex effects of electric current on precipitation is incomplete. For Alloy 617, this study shows electric current may impede precipitation at the interface. It should be noted that this retarding effect is also correlated to the temperature since precipitates at the interface were still seen in the EFAS samples fabricated at 1050 °C and 1100 °C. The retarding effect of current can be explained in Fig. 15a. In the beginning, Alloy 617 sheets were in contact and electric current was initiated to heat the sample. At the temperature of 1150 °C, precipitates were mostly eliminated from the interface. At the same time, grain growth occurred at elevated temperature. Since there were fewer precipitates to impede GB migration, greater GB migration was achieved.

High current density can enhance vacancy defect migration and thus improve atomic diffusion. Besides temperature which has been widely accepted to affect atomic diffusion,

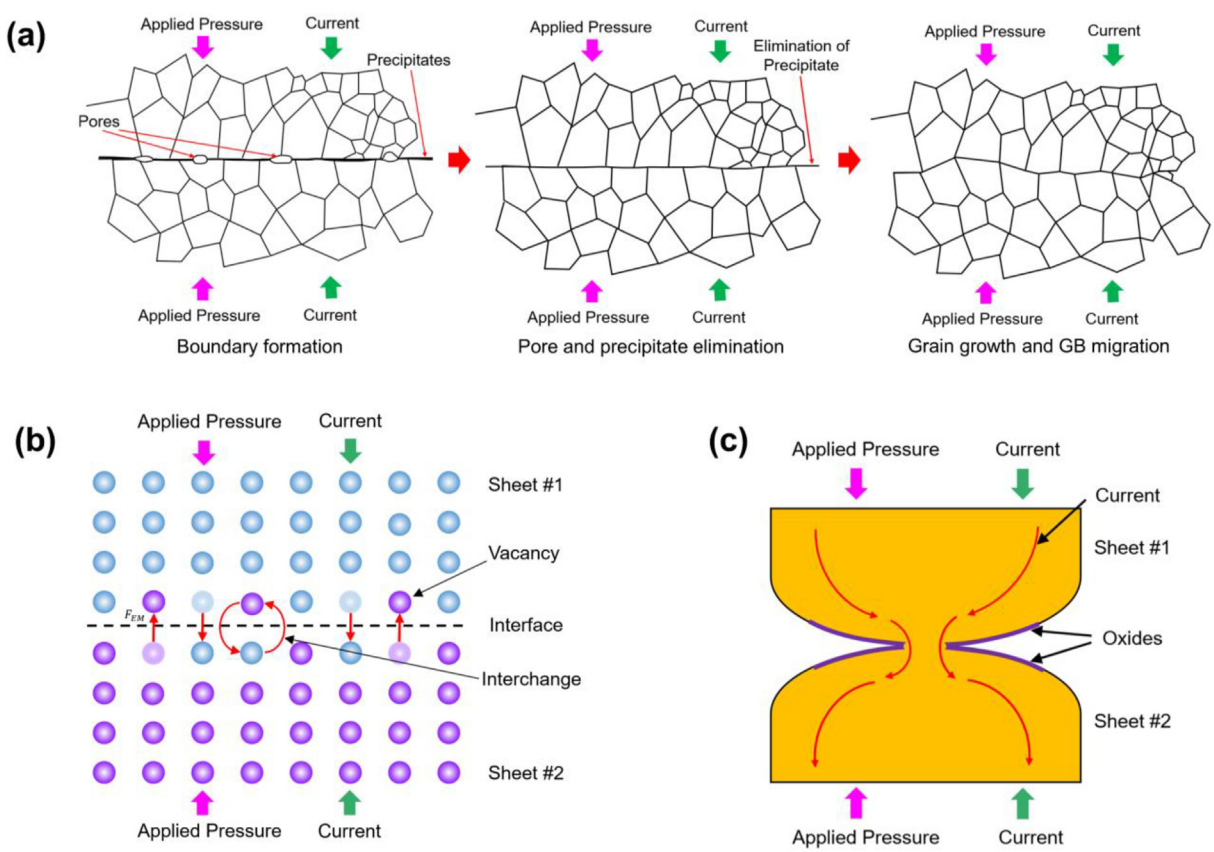

Fig. 15 – Schematics showing enhanced DB using EFAS by the mechanisms of (a) impeding precipitation at the interface, (b) enhancing vacancy defect migration, and (c) dielectric breakdown of surface oxides.

electric current may influence atomic diffusion. In traditional HP, the diffusion coefficient as a function of temperature can be expressed as.

$$D = D_0 \exp\left(-\frac{Q}{RT}\right) \quad (1)$$

where D_0 is the frequency factor (material constant), Q is the energy of formation of vacancies, R is the gas constant and T is the temperature. When an electric current is taken into account, the effective diffusion coefficient, D_{eff} can be written as [43]

$$D_{eff} = D_0 \exp\left(-\frac{Q}{RT} + \frac{A|Z^*|etj}{RT}\right) \quad (2)$$

where A is the constant, Z^* is the effective valence, e is the charge of an electron, t is the resistivity, and j is the current density. Eq. (2) expresses the coupled effects of temperature and current on diffusion. Studies have shown enhanced atomic diffusion under current. Li et al. [31] investigated the diffusion behavior in Al-Fe couple and observed that the diffusion coefficient under current was ~46 times higher than that without current. Deng et al. [43] also reported an increased interdiffusion coefficient with the increase of current density in EFAS of W-Ti system. It has long been believed that the underlying reason for enhanced diffusion under current is due to electromigration, which intensifies vacancy defect migration. Electromigration is a forced atomic diffusion process with the driving force arising from an electric field and current [44]. The driving force of atomic movement driven by the current can be written as [45]

$$F_{EM} = Z^* etj \quad (3)$$

Fig. 15b schematically shows current-induced vacancy defect migration. At high temperatures, the density of vacancies was increased. Meanwhile, due to the current, enhanced vacancy defect migration was induced, which contributed to diffusion kinetics and resulted in improved GB migration compared to the zero-current HP counterparts.

Another effect of the electric field is surface cleaning and dielectric breakdown of surface oxides (Fig. 15c). Researchers in EFAS of nanometric nickel particles reported that the electric field could initiate dielectric breakdown of the surface thin oxide layer through percolation of oxygen vacancies and the migration of oxygen away from the particle contact, which leads to the formation of necks and subsequent growth [46,47]. In another study, Nagae et al. [28] studied Al particles sintered with and without electric current. They show that the current could lead to the breakup of the oxide layer and better density and tensile strength. In this study, although there is no direct evidence of the current's effect on oxide breakdown, an oxide dissolution effect may exist.

4.3. *The impact of temperature*

The temperature was found to have a significant influence on precipitation, grain growth, and GB migration in DB of Alloy 617 using EFAS. A substantial number of precipitates formed after 30 min exposure at 1050 °C (EFAS-#1, Figs. 10a) and 1100 °C (EFAS-#3, Fig. 10c). Inversely, precipitates concentration decreased significantly in the sample fabricated at 1150 °C (EFAS-#8, Fig. 10h). The solution annealing temperature of Alloy 617 is ~1170 °C. Therefore, during EFAS at 1150 °C, the material experienced equivalent solution annealing heat treatment. As a result, most precipitates were dissolved into the Alloy 617 matrix. The subsequent fast cooling in the EFAS chamber prevented reprecipitation. The samples fabricated at 1050 °C and 1100 °C, however, departed the solution annealing temperature, and therefore extensive precipitates were formed.

Grain growth depends strongly on the temperature during DB. EFAS at 1050 °C and 1100 °C did not lead to noticeable grain growth compared to the as-received material (Figs. 11b, d and 3d). However, as the temperature increased to 1150 °C while keeping the pressure and hold time constant, grain growth was initiated and an average grain size ~5 times the as-received material was obtained (Fig. 11h). Grain growth is expected during DB. It was reported that substantial grain growth (293 ± 104 μm) was observed during HP at 1150 °C [8]. This grain size range is similar to the EFAS samples fabricated at 1150 °C in this study.

In addition to grain growth, temperature resulted in differences in GB migration across the DB interface. As shown in Figs. 10a and 11a, planar grain boundaries were found at the interface of the EFAS-#1. No GB migration was observed. As the temperature increased to 1100 °C, GB migration was initiated (Figs. 10c and 11e), although the amount of GB migration was very low. However, EFAS at 1150 °C resulted in excellent GB migration (88.5%) as seen in Fig. 11g, leaving the original interface barely visible. According to Eq. (1), the temperature is the main factor controlling diffusion coefficient. Diffusion improves as the temperature increases. DB temperature should be optimized since bonding at inappropriate high temperatures will fail due to excessive deformation (e.g., HP-#4). However, it should be emphasized that temperature alone does not result in excellent GB migration. This can be evidenced by HP-#4 (53.2%) and EFAS-#8 (88.5%) which have different diffusion qualities while both were made at equivalent temperature conditions. Literature also supports similar findings that limited GB migration was achieved using HP even at 1250 °C [11]. It is due to the precipitates at the interface of the HP samples which inhibited GB migration. It also needs to be noted that temperature is important for DB using EFAS. This is because EFAS at inappropriate temperatures (1050 °C and 1100 °C) failed to achieve good diffusion (Fig. 10a–c). This suggests that the electric current results in a temperature profile that plays a key role in the DB of Alloy 617.

4.4. *The impact of pressure*

The applied pressure in EFAS affects deformation and GB migration. This can be concluded by comparing EFAS-#4, #6, and #8, all were fabricated at 1150 °C for 30 min under varied pressure (#4: 10 MPa, #6: 20 MPa, #8: 30 MPa). The deformation of the sample increased from 3.1% to 23.1% as the pressure raised from 10 MPa to 30 MPa (Table 3). Pressure is responsible for achieving good contact with the sheets during DB. Minimal pressure is required to facilitate the local deformation of asperities to form a good contact while maximum pressure should be optimized to avoid excessive sample deformation. A previous study has reported that low pressure could lead to

pores and cavities during EFAS [48]. In this study, the EFAS sample fabricated at the lowest pressure (10 MPa) still showed good interfacial quality, indicating enough pressure to eliminate those pores along the interface.

The pressure benefited GB migration. Increasing the pressure from 10 MPa to 30 MPa at the same temperature (1150 °C) and hold time (30 min) enhanced GB migration from 52.7% (EFAS-#4) to 88.5% (EFAS-#8). Pressure favored GB migration due to the following three reasons. First, high pressure contributed to better surface contact of Alloy 617 sheets. In the case of powder materials, pressure provides an extrinsic driving force to contribute to powder shrinkage and accelerates the densification rate [49]. In DB of Alloy 617 sheets, the pressure also helped to deform local asperities and achieve better contact. Second, it is hypothesized that pressure-induced deformation helped break the oxides at the interface. Hence, the penetration of the oxide layer resulted in better diffusion. Third, the pressure elevated the atomic diffusion coefficient. Li et al. proposed the effective diffusion coefficient under pressure written as [50].

$$D^P = D_0^P \exp\left(-\frac{Q}{RT}\right) \tag{4}$$

where D^P is an extra diffusion coefficient resulting from the pressure and D_0^P is the item of increasing diffusion constant. The pressure intensified atomic diffusion and resulted in better GB migration.

4.5. *The impact of hold time*

Hold time is necessary for the diffusion process. When the mating surfaces contact, hold time is required to close the pores left at the interface. Insufficient hold time may result in remaining pores at the interface (e.g., HP-#3 with 30 min hold shows pores at the interface). The EFAS samples fabricated with 10 min dwell showed a porosity-free interface, indicating a 10 min hold is sufficient to eliminate the pores.

Hold time, coupled with temperature, affects deformation. An increase in deformation can be seen by extending the hold time from 10 min (EFAS-#5) to 30 min (EFAS-#6) and to 90 min (EFAS-#7), while the temperature (1150 °C) and pressure (20 MPa) are constant. Creep occurred during DB. A longer dwell led to more deformation of the material. A prolonged time also benefited GB migration. A ~20% improvement in GB migration was obtained by extending the time from 10 min (EFAS-#5) to 90 min (EFAS-#7). A longer hold at the target temperature gave more time for the diffusion to take place.

5. Conclusion

In this study, DB of Alloy 617 was performed using EFAS and HP under different conditions to study the influence of electric current, temperature, pressure, and hold time on the microstructure of diffusion-bonded Alloy 617. Based on the experimental results, the following conclusion can be drawn.

(1) Cr- and Mo-rich precipitates remained along the interface of the HP samples, which inhibited GB migration over the interface. Nanoscale Al-rich oxide also remained at the interface of the HP and EFAS samples. Grain boundary motion across the DB interface occurred with the presence of the nanoscale Al-oxide precipitates.
(2) The applied current and associated temperature during EFAS had an influence on precipitates and GB migration. At sufficient temperatures (1150 °C), EFAS successfully eliminated large precipitates at the interface and resulted in good GB migration across the DB interface.
(3) The temperature, pressure, and hold time are important factors during DB of Alloy 617 using EFAS. The temperature is a prerequisite for a successful GB migration. GB migration can be enhanced with the increase of pressure and hold time.

Declaration of competing interest

The authors declare that they have no known competing financial interests or personal relationships that could have appeared to influence the work reported in this paper.

Acknowledgments

This project was funded by the Idaho National Laboratory Laboratory-Directed Research & Development (LDRD) Program under the Department of Energy (DOE) Idaho Operations Office Contract DE-AC07-05-ID14517.

REFERENCES

[1] A.C. Dimian, C.S. Bildea, A.A. Kiss, Chapter 10 - process intensification, in: A.C. Dimian, C.S. Bildea, A.A. Kiss (Eds.), Computer aided chemical engineering, Elsevier2014, pp. 397-448.
[2] Mofid MA, Loryaei E. Investigating microstructural evolution at the interface of friction stir weld and diffusion bond of Al and Mg alloys. J Mater Res Technol 2019;8(5):3872–7.
[3] Mahajan HP, Elbakhshwan M, Beihoff BC, Hassan T. Mechanical and microstructural characterization of diffusion bonded 800H. ASME 2020 Pressure Vessels & Piping Conference; 2020.
[4] Xiong J, Yuan L, Zhu Y, Zhang H, Li J. Diffusion bonding of nickel-based superalloy GH4099 with pure nickel interlayer. J Mater Sci 2019;54(8):6552–64.
[5] Meng Y, Gu X, Cui M, Gu X, Zhao X. Laser assisted diffusion bonding of TC4 titanium alloy to 301 stainless steel using a Ni interlayer. J Mater Res Technol 2022;21:739–48.
[6] Xiao Y, Lang L, Xu W, Zhang D. Diffusion bonding of copper alloy and nickel-based superalloy via hot isostatic pressing. J Mater Res Technol 2022;19:1789–97.
[7] Sabetghadam H, Hanzaki AZ, Araee A. Diffusion bonding of 410 stainless steel to copper using a nickel interlayer. Mater Char 2010;61(6):626–34.
[8] Sah I, Kim D, Lee HJ, Jang C. The recovery of tensile ductility in diffusion-bonded Ni-base alloys by post-bond heat treatments. Mater Des 2013;47:581–9.
[9] Sah I, Kim E-S. Enhanced joint integrity of diffusion-welded Alloy 617 by controlling the micro-chemistry near the surface. Mater Today Commun 2021;29:102770.

[10] Sah I, Hwang J-B, Kim E-S. Creep behavior of diffusion-welded alloy 617. Metals 2021;11(5):830.
[11] Song CH, Cho IH, Choi JS. A study on diffusion bonding performance of inconel 617 heat exchanger. Int J Precis Eng Manuf 2015;16(5):957–63.
[12] Sah I, Hwang J-B, Kim W-G, Kim E-S, Kim M-H. High-temperature mechanical behaviors of diffusion-welded Alloy 617. Nucl Eng Des 2020;364:110617.
[13] Mylavarapu SK, Sun X, Christensen RN, Unocic RR, Glosup RE, Patterson MW. Fabrication and design aspects of high-temperature compact diffusion bonded heat exchangers. Nucl Eng Des 2012;249:49–56.
[14] Mylavarapu SK, Unocic RR, Xiaodong S, Christensen RN. On the microstructural and mechanical characterization of diffusion bonded Alloy 617 plate specimens for high-temperature compact heat exchangers. Trans Am Nucl Soc 2009;101:367–9.
[15] T.C. Totemeier, H. Tian, D.E. Clark, J.A. Simpson, Microstructure and strength characteristics of alloy 617 welds, United States, 2005.
[16] Li X, Smith T, Kininmont D, Dewson SJ. Materials for nuclear diffusion-bonded compact heat exchangers, Proceedings of 2009 international congress on advances in nuclear power plants. Japan. 2009. p. 2572.
[17] Li X, Kininmont D, Le Pierces R, Dewson SJ. Alloy 617 for the high temperature diffusion-bonded compact heat exchangers. United States: American Nuclear Society - ANS; 2008.
[18] Xiuqing L, Le Pierres R, Dewson SJ. Heat exchangers for the next generation of nuclear reactors. United States: American Nuclear Society - ANS; 2006.
[19] Cho IH, Song CH, Yoon SH, Park SJ. The study on bonding test of Inconel 617 heat exchanger by measuring properties, proceedings of the KNS 2014 spring meeting, KNS, korea. Republic of. 1CD-ROM; 2014.
[20] Hu Z-Y, Zhang Z-H, Cheng X-W, Wang F-C, Zhang Y-F, Li S-L. A review of multi-physical fields induced phenomena and effects in spark plasma sintering: fundamentals and applications. Mater Des 2020;191:108662.
[21] Lu J, Wang Q, Liu C, Zhang C, Chen D, Cui G. Cracking behavior of AISI 316L stainless steel powder by gas nitriding and its influence on spark plasma sintering. J Mater Res Technol 2022;20:3796–806.
[22] Yan S, Wang Q, Chen X, Zhang C, Cui G. Fabrication of highly compact Inconel 718 alloy by spark plasma sintering and solution treatment followed by aging. Vacuum 2019;163:194–203.
[23] Shongwe MB, Diouf S, Durowoju MO, Olubambi PA. Effect of sintering temperature on the microstructure and mechanical properties of Fe–30%Ni alloys produced by spark plasma sintering. J Alloys Compd 2015;649:824–32.
[24] Wang Z, Liu P, Wang A, Xie J, Hou B. Effect of spark plasma sintering temperature on the multi-scale microstructure evolution and mechanical properties of Ti2AlC/TiAl composites with network architecture. J Mater Res Technol 2023;25:6209–23.
[25] Yang J, Trapp J, Guo Q, Kieback B. Joining of 316L stainless steel by using spark plasma sintering method. Mater Des 2013;52:179–89.
[26] Zhao K, Liu Y, Huang L, Liu B, He Y. Diffusion bonding of Ti-45Al-7Nb-0.3W alloy by spark plasma sintering. J Mater Process Technol 2016;230:272–9.
[27] Ananthakumar K, Vivekanandhan P, Kumaran S. Spark plasma assisted diffusion bonding of titanium and stainless steel: role of pulse current in diffusion kinetics and microstructural evolution. Vacuum 2020;177:109394.
[28] Nagae T, Yokota M, Nose M, Tomida S, Kamiya T, Saji S. Effects of pulse current on an aluminum powder oxide layer during pulse current pressure sintering. Mater Trans 2002;43(6):1390–7.
[29] Li YY, Yang C, Qu SG, Li XQ, Chen WP. Nucleation and growth mechanism of crystalline phase for fabrication of ultrafine-grained Ti66Nb13Cu8Ni6.8Al6.2 composites by spark plasma sintering and crystallization of amorphous phase. Mater Sci Eng, A 2010;528(1):486–93.
[30] Yang C, Mo DG, Lu HZ, Li XQ, Zhang WW, Fu ZQ, et al. Reaction diffusion rate coefficient derivation by isothermal heat treatment in spark plasma sintering system. Scripta Mater 2017;134:91–4.
[31] Li R, Yuan T, Liu X, Zhou K. Enhanced atomic diffusion of Fe–Al diffusion couple during spark plasma sintering. Scripta Mater 2016;110:105–8.
[32] Salandro WA, Jones JJ, Bunget C, Mears L, Roth JT. The effect of electric current on metals. In: Salandro WA, Jones JJ, Bunget C, Mears L, Roth JT, editors. Electrically assisted forming: modeling and control. Cham: Springer International Publishing; 2015. p. 37–54.
[33] Kapoor R, Sunil S, Bharat Reddy G, Nagaraju S, Kolge TS, Sarkar SK, et al. Electric current induced precipitation in maraging steel. Scripta Mater 2018;154:16–9.
[34] Zhao Z, Wang G, Zhang Y, Wang Y, Hou H. Fast recrystallization and phase transformation in ECAP deformed Ti–6Al–4V alloy induced by pulsed electric current. J Alloys Compd 2019;786:733–41.
[35] Montes JM, Rodríguez JA, Cuevas FG, Cintas J. Consolidation by electrical resistance sintering of Ti powder. J Mater Sci 2011;46(15):5197–207.
[36] Tang W, Zhang L, Zhu J-f, Chen Y, Tian W, Liu T. Effect of direct current patterns on densification and mechanical properties of binderless tungsten carbides fabricated by the spark plasma sintering system. Int J Refract Metals Hard Mater 2017;64:90–7.
[37] Bernardo MS, Jardiel T, Caballero AC, Bram M, Gonzalez-Julian J, Peiteado M. Electric current activated sintering (ECAS) of undoped and titanium-doped BiFeO3 bulk ceramics with homogeneous microstructure. J Eur Ceram Soc 2019;39(6):2042–9.
[38] Narayan Singh A, Moitra A, Bhaskar P, Sasikala G, Dasgupta A, Bhaduri AK. Effect of thermal aging on microstructure, hardness, tensile and impact properties of Alloy 617. Mater Sci Eng, A 2018;710:47–56.
[39] Akbari-Garakani M, Mehdizadeh M. Effect of long-term service exposure on microstructure and mechanical properties of Alloy 617. Mater Des 2011;32(5):2695–700.
[40] Properties of Inconel alloy 617. 2005. https://www.specialmetals.com/documents/technical-bulletins/inconel/inconel-alloy-617.pdf.
[41] Onodera Y, Hirano KI. The effect of direct electric current on precipitation in a bulk Al-4 wt % Cu alloy. J Mater Sci 1976;11(5):809–16.
[42] Shine MC, Herd SR. Effect of direct current on precipitation in quenched Al + 4% Cu thin films. Appl Phys Lett 1972;20(6):217–9.
[43] Deng S, Li R, Yuan T, Xie S, Zhang M, Zhou K, et al. Direct current-enhanced densification kinetics during spark plasma sintering of tungsten powder. Scripta Mater 2018;143:25–9.
[44] Deng S, Yuan T, Li R, Zhang M, Xie S, Wang M, et al. Influence of electric current on interdiffusion kinetics of W-Ti system during spark plasma sintering. Int J Refract Metals Hard Mater 2018;75:184–90.
[45] Tan CM, Roy A. Electromigration in ULSI interconnects. Mater Sci Eng R Rep 2007;58(1):1–75.
[46] Bonifacio CS, Rufner JF, Holland TB, Benthem Kv. In situ transmission electron microscopy study of dielectric

breakdown of surface oxides during electric field-assisted sintering of nickel nanoparticles. Appl Phys Lett 2012;101(9):093107.
[47] Bonifacio CS, Holland TB, van Benthem K. Time-dependent dielectric breakdown of surface oxides during electric-field-assisted sintering. Acta Mater 2014;63:140–9.
[48] Ogneva TS, Bataev IA, Mali VI, Anisimov AG, Lazurenko DV, Popelyukh AI, et al. Effect of sintering pressure and temperature on structure and properties of NiAl metal-intermetallic composites produced by SPS. Mater Char 2021;180:111415.
[49] Alaniz JE, Dupuy AD, Kodera Y, Garay JE. Effects of applied pressure on the densification rates in current-activated pressure-assisted densification (CAPAD) of nanocrystalline materials. Scripta Mater 2014;92:7–10.
[50] Li XX, Yang C, Chen T, Fu ZQ, Li YY, Ivasishin OM, et al. Effective atomic diffusion coefficient dependence on applied pressure during spark plasma sintering. Materialia 2019;6:100334.